Evaluation of musculoskeletal phenotype of the G608G progeria mouse model with lonafarnib, pravastatin, and zoledronic acid as treatment groups

Maria B. Cubria[a,1], Sebastian Suarez[a,1], Aidin Masoudi[a], Ramin Oftadeh[a,b], Pramod Kamalapathy[a], Amanda DuBose[c], Michael R. Erdos[c], Wayne A. Cabral[c], Lamya Karim[d], Francis S. Collins[c], Brian D. Snyder[a,e], and Ara Nazarian[a,f,2]

[a]Center for Advanced Orthopaedic Studies, Beth Israel Deaconess Medical Center, Boston, MA 02215; [b]Department of Biological Engineering, Massachusetts Institute of Technology, Cambridge, MA 02139; [c]Medical Genomics and Metabolic Genetics Branch of the National Human Genome Research Institute, National Institutes of Health, Bethesda, MD 20892; [d]Department of Bioengineering, University of Massachusetts, Dartmouth, MA 02747; [e]Department of Orthopedic Surgery, Boston Children's Hospital, Boston, MA 02115; and [f]Department of Orthopaedic Surgery, Yerevan State Medical University, 0025 Yerevan, Armenia

Edited by David A. Weitz, Harvard University, Cambridge, MA, and approved April 1, 2020 (received for review April 25, 2019)

Hutchinson–Gilford progeria syndrome (HGPS) is a uniformly fatal condition that is especially prevalent in skin, cardiovascular, and musculoskeletal systems. A wide gap exists between our knowledge of the disease and a promising treatment or cure. The aim of this study was to first characterize the musculoskeletal phenotype of the homozygous G608G BAC-transgenic progeria mouse model, and to determine the phenotype changes of HGPS mice after a five-arm preclinical trial of different treatment combinations with lonafarnib, pravastatin, and zoledronic acid. Microcomputed tomography and CT-based rigidity analyses were performed to assess cortical and trabecular bone structure, density, and rigidity. Bones were loaded to failure with three-point bending to assess strength. Contrast-enhanced μCT imaging of mouse femurs was performed to measure glycosaminoglycan content, thickness, and volume of the femoral head articular cartilage. Advanced glycation end products were assessed with a fluorometric assay. The changes demonstrated in the cortical bone structure, rigidity, stiffness, and modulus of the HGPS G608G mouse model may increase the risk for bending and deformation, which could result in the skeletal dysplasia characteristic of HGPS. Cartilage abnormalities seen in this HGPS model resemble changes observed in the age-matched WT controls, including early loss of glycosaminoglycans, and decreased cartilage thickness and volume. Such changes might mimic prevalent degenerative joint diseases in the elderly. Lonafarnib monotherapy did not improve bone or cartilage parameters, but treatment combinations with pravastatin and zoledronic acid significantly improved bone structure and mechanical properties and cartilage structural parameters, which ameliorate the musculoskeletal phenotype of the disease.

Hutchinson–Gilford progeria syndrome | farnesyltransferase inhibitor | bisphosphonate | statin | cartilage volume

Hutchinson–Gilford progeria syndrome (HGPS) is a uniformly fatal condition that causes a dramatic acceleration of symptoms associated with aging, especially cardiovascular and cerebrovascular events that lead to premature death at ∼13 y of age (1). HGPS primarily affects the musculoskeletal and vascular systems as evidenced by skeletal dysplasia, joint contractures, scleroderma-like skin, lipoatrophy, alopecia, atherosclerosis, and severe failure to thrive (1, 2). It is a rare sporadic autosomal dominant disorder caused by a de novo heterozygous mutation in the LMNA gene (c.1824C > T, p.G608G) (3, 4). The LMNA gene encodes for lamins type A and C and is composed of 12 exons (5). Prelamin A, the precursor protein of lamin A, undergoes posttranslational processing on its C-terminal region. Posttranslational modifications include transient farnesylation of the cysteine at the C-terminal CaaX motif, followed by proteolytic cleavage of the last three amino acids (aaX) by the metalloproteinase ZMPSTE24, and carboxymethylation. Finally, ZMPSTE24 performs an additional cleavage of the last 15 amino acids in the C-terminal region, which results in removal of the farnesyl group (4). These posttranslational modifications lead to the mature unfarnesylated lamin A protein (6, 7). Lamin A is predominantly an inner nuclear membrane protein that broadly influences nuclear structure and function (8). In addition, a small fraction of lamin A has been described to reside as a highly dynamic pool in the nucleoplasm (9–12). The posttranslational processing previously mentioned (farnesylation and carboxymethylation of the cysteine residue and removal of the -AAX tripeptide) appears to be important for the close association of lamins with the inner nuclear membrane (9, 13–15).

In HGPS, a single C-to-T transition occurs at position 1824 in the LMNA gene (c.1824C > T, p.G608G), activating a cryptic splice site that deletes the terminal 150 nucleotides of exon 11. This leads to a 50-amino acid deletion in the C-terminal domain of prelamin A, which eliminates the second endoproteolytic cleavage site, resulting in a truncated and permanently farnesylated protein termed progerin or LMNAΔ50 (16). Persistent farnesylation

Significance

We outline the musculoskeletal phenotype in a Hutchinson–Gilford progeria syndrome (HGPS) mouse model (G608G) that accurately simulates the changes found in humans with this disease, to evaluate the effects of treatments on natural course of the disease. As cartilage abnormalities seen in this HGPS model resemble those observed in the age-matched WT controls, further studies at different growth stages would allow researchers to understand cartilage health and structure to determine whether cartilage degeneration in these mice is attributable to premature aging of the tissue or due to a developmental alteration. This raises the possibility of using these mice as a model resembling degenerative joint disease in the elderly, toward early detection, management, and development of novel therapeutics for osteoarthritis.

Author contributions: M.B.C., S.S., A.D., M.R.E., W.A.C., F.S.C., B.D.S., and A.N. designed research; M.B.C., S.S., A.M., R.O., P.K., A.D., M.R.E., W.A.C., L.K., F.S.C., B.D.S., and A.N. performed research; M.B.C., S.S., R.O., P.K., A.D., M.R.E., W.A.C., L.K., F.S.C., B.D.S., and A.N. analyzed data; and M.B.C., S.S., A.D., M.R.E., W.A.C., L.K., F.S.C., B.D.S., and A.N. wrote the paper.

The authors declare no competing interest.

This article is a PNAS Direct Submission.

Data deposition: All data are available at the Open Science Framework (https://osf.io/u6p3c/).

[1]M.B.C. and S.S. contributed equally to this work.

[2]To whom correspondence may be addressed. Email: anazaria@bidmc.harvard.edu.

First published May 13, 2020.

causes progerin accumulation in the inner nuclear membrane, which is at least partly responsible for the HGPS phenotype (17).

Preclinical and clinical studies have been conducted with three different upstream prenylation inhibitors, including lonafarnib, pravastatin, and zoledronate. Lonafarnib is a farnesyltransferase inhibitor (FTI) that binds reversibly to the farnesyltransferase binding site (18) and therefore inhibits progerin farnesylation. FTIs have been shown to improve weight, arterial pulse wave velocity, carotid artery echo density, skeletal rigidity, and sensorineural hearing in children with HGPS (19). Furthermore, transgenic HGPS murine models treated with FTIs have shown improvement in cardiovascular defects (20), bone mineralization, and weight, as well as lifespan extension (21, 22).

Although FTIs have been previously shown to increase mean survival in HGPS patients (23–25), alternative prenylation events of progerin upstream of its farnesylation step were previously described, and can still occur in the presence of FTIs. Protein prenylation consists of the addition of farnesyl or geranylgeranyl groups on specific cysteine residues located near the C termini of various proteins (26). Alternative posttranslational prenylation of progerin (and subsequent accumulation) can occur by the action of the geranylgeranlyltransferase I (GGT-type I) protein. Hence, researchers have hypothesized that acting on the synthetic pathway of farnesyl phosphate (cosubstrate of farnesyltransferase and precursor of GGT-type I) would minimize alternative prenylation events and excess accumulation of progerin (7). The addition and synergistic action of other prenylation (including farnesylation or geranylgeranylation) inhibitors to the treatment strategy in HGPS patients has resulted in the addition of statins and bisphosphonates (23).

The statin pravastatin inhibits HMG-CoA reductase, while zoledronic acid inhibits farnesyl-pyrophosphate synthase. Inhibition of all three enzymes can effectively block the farnesylation step of progerin, and therefore halt its subsequent intercalation into the nuclear membrane (23, 24). Even though children with HGPS showed increased bone mineral density when treated with a combination of these drugs (24), other benefits are yet to be determined.

In the past two decades, several mouse models have been developed in order to test promising therapeutic options. Currently, there are seven *LMNA* and three *ZMPSTE24* genetically modified models (5, 6). One of the first *LMNA* mutant mouse models developed a myopathic phenotype that resembles the human Emery–Dreifuss muscular dystrophy, a disease in connection with HGPS. This model shows a severely decreased postnatal growth rate and evidence of cardiac and skeletal muscular dystrophy (27), including dystrophic perivertebral and lower limb muscles, as well as severely compromised ventricular heart fibers. Another mouse model for Emery–Dreifuss muscular dystrophy was developed in 2003 by introducing a nucleotide base change into the *LMNA* gene (28). It exhibits short stature, abnormal gait, micrognathia, abnormal dentition, scleroderma like skin, absence of subcutaneous fat, and musculoskeletal and heart muscle atrophy.

HGPS is a sporadic autosomal dominant syndrome and nearly 90% of the patients affected carry a de novo G608G heterozygous (c.1824C > T, p.G608G) mutation within exon 11 of *LMNA* (5, 29). In 2006, Varga et al. (30) published a detailed characterization of the vascular system in a heterozygous (p.G608G/+) HGPS mouse model. This mouse, heterozygous for a human transgene with the G608G mutation in *LMNA*, exhibits the progressive vascular abnormalities that closely resemble the most lethal aspect of the human HGPS phenotype. By 12 mo of age, aortic and carotid calcification, severe loss of vascular smooth muscle cells, thickening of the adventitia and middle layer of vessels, collagen deposition, and elastic fiber breakage were observed. Although G608G heterozygous transgenic mice develop pathologic changes in the medial layer of large vessels in a pattern very similar to that seen in children with HGPS, they lack the pathologic features of HGPS outside of the vascular system (external phenotype) seen in human patients (30).

In order to recapitulate bone microstructural and mechanical abnormalities observed in HGPS patients, several animal models of laminopathies have been generated. The first one reported is the *Zmpste24*$^{-/-}$ mouse. The bone phenotype in this animal model shows the development of kyphosis by 6 to 7 wk of age, and spontaneous bone fractures in multiple locations. Fractures of almost all ribs are apparent at 24 to 30 wk of age, although other fracture sites, such as the scapula, clavicle, sternum, zygomatic arch, mandible, and humerus have been reported as well (6, 31). Moreover, thoracic vertebrae exhibit reduced bone density, bone volume fraction (ratio of bone volume to total volume BV/TV), trabecular thickness, and increased porosity. In addition, cortical thickness values are reduced in the long bones of *Zmpste24*$^{-/-}$ mice.

More recently, the Lmna$^{G609G/G609G}$ homozygous animal model was generated, exhibiting joint immobility and skeletal deformities in the vertebral column (lordo-kyphosis) and the skull. In addition, tibias of the G609G mutant mice show decreased cortical bone mineral density, cortical thickness, and increased porosity (6).

As previously mentioned, the single base substitution at exon 11 of the LMNA gene is the most common mutation responsible for most of the HGPS cases observed in patients (5). As the heterozygous G608G mouse model (p.G608G/+) strictly focuses on the cardiovascular phenotype of the disease, the G608G transgene was recently bred to homozygosity, resulting in an HGPS mouse model that replicates many aspects of both musculoskeletal and vascular changes of HGPS human patients. This homozygous transgenic model expressing the human mutation includes a highly progressive vascular smooth muscle cells loss and large vessel calcification, as well as other features of HGPS not evident in the heterozygous transgenic model, such as kyphosis, joint contractures, craniofacial anomalies, severe lipodystrophy, skin tightening, and hair loss.

To date, there is no available description of the musculoskeletal phenotype in the HGPS homozygous G608G mouse model. Moreover, there is limited literature describing cartilage structural abnormalities and extracellular matrix (ECM) changes observed in animal models of HGPS disease. An HGPS mouse model that properly mimics the musculoskeletal changes in humans would be essential to assess new therapeutic strategies and evaluate how different treatments may alter the natural course of the disease. Therefore, we aimed to first characterize the musculoskeletal and cartilage phenotype of the homozygous G608G mouse model, and assess whether these changes can be used as an "assay" to track disease severity in HGPS patients. In addition, our secondary aim was to determine the phenotype changes of HGPS transgenic mice after a preclinical trial of different treatment combinations with lonafarnib, pravastatin, and zoledronic acid, and observe whether the combination of drugs ameliorate the disease phenotype. We hypothesized that: 1) Treatment with lonafarnib monotherapy will result in a nondetectable effect in bone tissue; 2) the addition of prenylation inhibitors that target bone resorption and stimulate bone tissue formation will synergistically improve the musculoskeletal phenotype of the homozygous G608G mouse model; and 3) combining bone protective medications with lonafarnib will still improve the disease phenotype and ameliorate the musculoskeletal abnormalities.

Research Design and Methods

Generation and characterization of LMNA G608G mice has been previously described (32). Animal care was provided at the NIH after Institutional Animal Care and Use Committee approval. These mice grew at a reduced rate for approximately 4 mo. They ate normally until 7 mo of age, where attentiveness and activity declined, causing progressive deterioration until premature death.

We conducted a five-arm preclinical trial consisting of: 1) HGPS homozygous transgenic mice treated with lonafarnib alone (P1L, $n = 4$); 2) HGPS

homozygous transgenic mice treated with pravastatin and zoledronic acid (P2PZ, $n = 5$); 3) HGPS homozygous transgenic mice treated with lonafarnib, pravastatin, and zoledronic acid (P3LPZ, $n = 5$); 4) HGPS homozygous transgenic mice with no treatment (HGPS-Ctrl, $n = 5$); and 5) age-matched C57BL/6 WT mice (8mWT, $n = 5$). The HGPS-Ctrl mice without treatment had age-matched WT mice littermates that were euthanized at the same time points as the HGPS mice. These age-matched WT mice were considered the "older WT healthy control mice." As the reported lifespan for the G608G homozygous model is ∼8 mo (33), we refer to these age-matched controls as the 8-mo-old WT mice (8mWT). In addition, 2-mo-old C57BL/6 WT mice (2mWT, $n = 10$) were included to determine whether any differences due to drug therapies cause musculoskeletal changes that trend toward older age-matched or younger healthy WT mice.

We randomly assigned diseased mice into one of four treatment groups (P1L, P2PZ, P3LPZ, or no treatment), where treatment was started at 2 mo of age. Lonafarnib (Schering-Plough) and pravastatin (Ranbaxy Pharmaceuticals Inc.) were mixed with transgenic dough at a concentration of 450-mg/kg and 100-mg/kg dough, respectively. A daily 5-g ball of dough, mixed with lonafarnib and/or pravastatin, was administered to each mouse. Food coloring was added for identification and to ensure even mixing. Zoledronic acid (Reclast, Novartis) was administered by intraperitoneal injections at 0.1 μg per gram of body weight per day. Control animals were given a daily 5-g ball of dough, without any drug. Transgenic mice were euthanized upon reaching severe pathology (loss of ≥15% body weight) together with their age-matched WT littermates. In addition, young WT mice were humanely euthanized at 2 mo of age (2mWT). Femurs were dissected and stripped of soft tissue, flash-frozen in liquid nitrogen, and stored at −80 °C until analysis.

Bacterial Artificial Chromosome G608G Transgenic Construct. The original bacterial artificial chromosome (BAC) clone RP11-702H12 (RPCI-11 Human BAC Library) was recombineered to contain a human insert with 164.4 kb of genomic DNA from chromosome 1q, including the *LMNA* gene with the G608G homozygous mutation, surrounding upstream and downstream elements (homology arms) from introns 10 and 11 of the *LMNA* gene, and four other known genes: *UBQLN4*, *MAPBPIP*, *RAB25*, and *MEX3A*. As previously described (30, 32), the BAC clone RP11-702H12 was recombineered to contain the most common mutation that causes HGPS, a C > T transition at base 1824 in LMNA exon 11. The final circular BAC G608G transgenic construct (total size with vector, 173.2 kb) was microinjected to create the G608G homozygous transgenic mouse line.

Assessment of Bone Structure, Density, and Rigidity. We obtained sequential transaxial images through the bone cross-section using microcomputed tomography (μCT) (μCT40, Scanco Medical). The samples were scanned using an integration time of 200 ms and a tube voltage and current of 70 kV and 114 mA, respectively. Cortical and trabecular structural indices were measured for each femur sample, as observed in Table 1. Cortical bone area (BA, mm^2), total area (TA, mm^2), cortical thickness (Ct.Th, mm), bone area fraction (BA/TA, %), and apparent and mineral density (MinDens, mg/cm^3) were measured for cortical bone specimens. Bone volume fraction (BV/TV, %), bone surface density (BS/BV, mm^{-1}), connectivity density (ConnD, mm^{-3}), Structure Model Index (SMI), trabecular number (Tb.N, mm^{-1}), trabecular thickness (Tb.Th, mm), trabecular spacing (Tb.Sp, mm), apparent and mineral densities, and degree of anisotropy (DA) were calculated for trabecular bone specimens. Volumetric bone mineral density (vBMD, $g{\cdot}cm^3$) was calculated using manufacturer-supplied hydroxyapatite phantoms to convert X-ray attenuation to a known MinDens. CT-based rigidity analysis (CTRA) was used to calculate the axial (EA, N), bending (EI, $N{\cdot}mm^{-2}$), and torsional (GJ, $N{\cdot}mm^{-2}$) rigidities for each transaxial cross-sectional image of each femur (2, 19, 34).

Axial and coronal μCT projections of the femurs were reconstructed using ImageJ (NIH) (35, 36) to evaluate the presence of coxa magna (enlargement of the femoral head with >10% asymmetry in size) and coxa valga (femoral neck shaft angle >125°), respectively. Femoral head area (FHA) was calculated in the axial cross-sections of the proximal and distal thirds of the femoral head to determine the presence of coxa magna. Moreover, the femoral neck shaft angle (NSA) was measured as the angle formed by the intersection of a line connecting the midpoints along the femoral shaft and another line connecting the midpoints of the femoral neck to evaluate the presence of coxa valga.

Mechanical Testing. Three-point bending was performed on the femurs using a MTS200 Synergy (MTS Inc.) load frame under displacement control conditions with an 8-mm support span. Specimens were thawed to room temperature and rehydrated for 30 min prior to testing. They were loaded to failure at an axial strain rate of 0.01 $mm{\cdot}s^{-1}$. Yield and ultimate load, displacement, stress, and strain, and flexural modulus were calculated using μCT-based area moment of inertia measures and an in-house developed MATLAB program (MathWorks).

Measurement of Glycosaminogylcan Content, Cartilage Thickness, and Volume. Contrast-enhanced microcomputed tomography (CECT) imaging of mouse femurs was performed to measure the glycosaminogylcan (GAG) content of the femoral head articular cartilage. We used an anionic iodinated contrast agent (Hexabrix 320; Mallinckrodt) that alters the X-ray attenuation of the cartilage in inverse proportion to cartilage GAG concentration. Femurs were placed overnight in a solution of Hexabrix at 12 mg I/mL before μCT imaging (70 Kvp, 113 μA, 0.006-μm voxel size, 30 slices). Postprocessing (Analyze TM, Mayo Clinic, Rochester, MN) consisted of segmenting cartilage from bone based on an X-ray attenuation gradient algorithm, and subtracting the average X-ray attenuation of the unenhanced cartilage at baseline from the contrast enhanced X-ray attenuation.

In order to quantitatively assess degradation of femoral articular cartilage, we calculated the thickness (mm^2) and volume (mm^3) for each specimen. First, axial projections of the femoral head were reconstructed using ImageJ to assess the thickness of the femoral articular cartilage. Cartilage thickness was then measured in three specific cross sections: one-third, one-half, and two-thirds of the femoral head height. Initial assessment was performed using Analyze TM by contouring the cartilage-contrasted area in the axial plane from the μCT scans, taking as reference the 45% of the femoral head height and analyzing 15 slices before and after this point for a precise and reproducible comparison. Measurements were then obtained at the thickest portion in the midpoint of the head at each cross section. Second, a three-dimensional (3D) cartilage volume assessment was performed using ScanIP (Simpleware, Synopsis, Software v2016.09). Finally, a complete 3D reconstruction of the femoral heads was performed contouring all three planes (axial, sagittal, and coronal) of each μCT scan slice.

Assessment of Advanced Glycation End Products in Bone. Bone proteins from the femoral diaphysis were extracted using established protocols (37, 38) and used for collagen and advanced glycation end product (AGE) measurement by a fluorometric assay following established methods (38–41). Briefly, bone samples were lyophilized and hydrolyzed according to dry mass in 6N HCl for 20 h at 110 °C. AGE bulk fluorescence (relative to a quinine standard) was measured from the hydrolysates at 360-nm/460-nm excitation/emission using a multimode spectrophotometer (SynergyMX, BioTek) and was normalized to collagen content per specimen. The amount of collagen per sample was determined based on hydroxyproline quantity (relative to a hydroxyproline standard) assessed by absorbance measurements of processed specimens at 570 nm using the same spectrophotometer (42).

Statistical Methods. Normality was assessed with the Shapiro–Wilk test. Survival analysis was conducted with a log-rank (Mantel-Cox) test. An ANOVA test was used to assess differences between animal groups and geometric, densitometric, structural, microstructural, biomechanical, and mechanical indices as dependent variables; a post hoc Bonferroni test was used to detect differences within groups. For outcomes that did not meet the normality assumption, we performed a Kruskall–Wallis test with post hoc multiple comparisons. All reported outcomes were independent of body mass index, which was not accounted for in the analysis. Sex-adjusted differences within treatment arms were calculated with an unpaired *t* test or Wilcoxon rank sum test. Two-tailed *P* values less than 0.05 were considered significant. Statistical analyses were conducted with RStudio v1.0.153 (RStudio) (43, 44). Normality assumption was met only by FHA, NSA, and trabecular BS/BV. Mean and SDs were used to report normally distributed outcomes; median and interquartile ranges were used for nonnormally distributed variables. Reported *P* values in Tables 1 and 2 can be interpreted as: 1) *P* values in 8mWT column: 8mWT vs. 2mWT mice; 2) *P* values in HGPS-Ctrl: HGPS Ctrl vs. 8mWT mice; 3) *P* values under P1L, P2PZ, and P3LPZ: each treatment arm independently vs. HGPS-Ctrl mice.

Data Availability Statement. All data from this manuscript are available at the Open Science Framework (https://osf.io/u6p3c/).

Results

Nineteen transgenic and 15 WT mice were included in the study, of which 10 were 2mWT and 5 were age-matched WT mice (8mWT). A total of 44 femurs were analyzed, of which 24 were

Table 1. Cortical and trabecular structural indices of mouse femurs (measurements are reported as medians and interquartile ranges)

	2mWT	8mWT	HGPS-Ctrl	P1L	P2PZ	P3LPZ
n (%)	20 (45.5)	5 (11.4)	5 (11.4)	4 (9.1)	5 (11.4)	5 (11.4)
Cortical structure						
BA/TA (%)	0.990 (0.987–0.990)	0.996 (0.995–0.996)	0.996 (0.995–0.996)	0.996 (0.996–0.996)	0.997 (0.997–0.997)	0.997 (0.997–0.997)
P value		**0.008**	0.458	0.250	0.099	0.196
Ct.Th	0.12 (0.11–0.12)	0.19 (0.16–0.19)	0.16 (0.14–0.16)	0.12 (0.12–0.13)	0.23 (0.22–0.24)	0.19 (0.19–0.24)
P value		**0.002**	0.197	0.135	**0.044**	0.083
AppDens (mg/cm^3)	969.35 (960.93–978.90)	1153.68 (1118.63–1165.93)	1134.85 (1100.98–1135.35)	984.22 (972.41–1028.95)	1165.03 (1089.62–1184.49)	1147.19 (1139.08–1191.70)
P value		**<0.001**	0.284	0.156	0.276	0.186
MinDens (mg/cm^3)	996.02 (988.05–1006.61)	1185.57 (1149.99–1197.19)	1166.29 (1134.72–1167.82)	1004.22 (992.01–1053.18)	1190.98 (1110.44–1210.26)	1177.19 (1166.29–1216.83)
P value		**<0.001**	0.331	0.106	0.322	0.249
Trabecular structure						
BV/TV (%)	0.12 (0.11–0.13)	0.05 (0.04–0.05)	0.03 (0.02–0.06)	0.01 (0.01–0.02)	0.16 (0.13–0.16)	0.16 (0.15–0.21)
P value		**0.005**	0.439	0.329	**0.004**	**<0.001**
BS/BV (1/mm)*	72.89 ± 6.07	51.64 ± 4.17	66.22 ± 4.91	60.57 ± 10.13	53.23 ± 9.63	52.79 ± 18.76
P value		**<0.001**	0.482	1.000	0.819	0.709
Tb.N (1/mm)	5.09 (4.40–5.39)	2.07 (2.00–2.53)	2.32 (2.10–3.10)	1.55 (1.15–1.83)	3.90 (3.34–4.92)	4.83 (4.63–5.49)
P value		**<0.001**	0.406	0.293	0.094	**0.014**
Tb.Th (58)	0.04 (0.04–0.04)	0.06 (0.06–0.06)	0.04 (0.04–0.05)	0.06 (0.06–0.06)	0.05 (0.04–0.06)	0.04 (0.04–0.08)
P value		**<0.001**	0.294	0.317	0.458	0.430
Tb.Sp (58)	0.20 (0.18–0.23)	0.49 (0.40–0.50)	0.43 (0.34–0.48)	0.56 (0.52–0.61)	0.25 (0.20–0.30)	0.20 (0.17–0.24)
P value		**<0.001**	0.374	0.325	0.086	**0.017**
SMI	2.02 (1.82–2.16)	2.61 (2.45–2.66)	3.24 (2.78–3.74)	3.76 (3.02–4.60)	1.87 (1.59–2.07)	1.74 (1.21–1.74)
P value		**0.004**	0.404	0.486	**0.004**	**<0.001**
ConnD ($1/mm^3$)	299.71 (267.09–319.94)	21.77 (14.75–24.27)	8.63 (4.75–53.45)	1.04 (0.45–2.15)	80.75 (77.07–292.86)	165.56 (107.70–301.06)
P value		**<0.001**	0.494	0.305	0.106	0.051
AppDens (mg/cm^3)	116.95 (97.94–124.04)	54.47 (35.55–61.14)	35.71 (19.23–67.47)	62.83 (51.17–69.59)	112.22 (108.16–147.17)	154.74 (86.27–155.19)
P value		**0.002**	0.442	0.446	**0.034**	**0.009**
MinDens (mg/cm^3)	729.71 (725.32–734.40)	849.89 (824.75–852.86)	797.01 (794.75–851.65)	878.99 (845.97–879.89)	869.35 (851.42–881.33)	829.17 (826.92–934.58)
P value		**0.001**	0.425	0.341	0.237	0.281
DA	1.921 (1.900–1.956)	1.143 (1.115–1.201)	1.280 (1.195–1.288)	1.336 (1.232–1.391)	1.278 (1.213–1.312)	1.472 (1.152–1.625)
P value		**<0.001**	0.242	0.380	0.461	0.407

P values represent statistical significance of differences among groups; multiple comparisons are included in the text. AppDens apparent density; BA/TA; bone area fraction; BS/BV, bone surface density; BV/TV, bone volume fraction; ConnDens, connectivity density; Ct.Th, cortical thickness; DA, degree of anisotropy; MinDens, mineral density; SMI, structural model index; Tb.N trabecular number; Tb.Sp, trabecular spacing; Tb.Th, trabecular thickness. Bold values demonstrate significance.
*These measurements are reported as mean and SD

the left femurs from transgenic and 8mWT mice and 20 were bilateral femurs from 2mWT mice.

HGPS control (Ctrl) mice had age-matched WT mice littermates that were euthanized at the same time points as HGPS mice. These age-matched controls are considered the "older healthy WT mice" or "8mWT," as referred to in this section.

The mean age at death for HGPS mice was 39.4 wk (SD = 6.2 wk). Overall, no significant differences were observed in survival rates between treatment groups ($\chi^2 = 5.9$, $P = 0.114$) as observed in Fig. 1. However, survival rates were significantly higher for male than for female HGPS mice ($\chi^2 = 5.7$, $P = 0.017$). Sex-adjusted differences in age at death within treatment groups are shown in Table 3.

Results for bone and cartilage parameters will be reported as follows: 1) Progeria-Ctl vs. age-matched WT mice (HGPS-Ctrl vs. 8mWT mice); 2) progeria-treated mice (P1L, P2PZ, and P3LPZ) vs. HGPS-Ctrl; and 3) physiological aging assessment: 2mWT vs. 8mWT mice. In addition, gender differences (female vs. male mice in each condition) will be reported at the end of each section.

Cortical Bone Material Properties: Thickness, BA/TA, and MinDens. HGPS-Ctrl mice showed a 15% decrease in Ct.Th when compared to 8mWT mice ($P = 0.197$). There was a 44% increase ($P = 0.044$) in bone Ct.Th when mice were treated with zoledronic acid and pravastatin (P2PZ group) when compared to the HGPS-Ctrl group. The 8mWT mice showed a 58% increase in Ct.Th when compared to 2mWT mice ($P = 0.002$) (Table 1). No significant changes occurred in cortical BA/TA in all treatment conditions, as seen in Table 1.

Table 2. Mechanical testing, femoral geometry, and cartilage parameters (measurements are reported as medians and interquartile ranges)

Outcome	2mWT	8mWT	HGPS-Ctrl	P1L	P2PZ	P3LPZ
n (%)	20 (45.5)	5 (11.4)	5 (11.4)	4 (9.1)	5 (11.4)	5 (11.4)
Mechanical testing						
Yield stress	157.2	150.3	205.6	161.4	211.6	199.5
(MPa)	(136.3–169.8)	(132.5–165.3)	(130.0–208.1)	(149.7–194.4)	(208.6–228.2)	(182.7–219.3)
P value		0.434	0.114	0.368	0.091	0.163
Ultimate stress	164.45	157.42	213.02	169.49	228.17	219.26
(MPa)	(152.09–184.54)	(143.48–169.72)	(173.90–216.28)	(164.48–183.67)	(212.96–231.15)	(188.45–231.97)
P value		0.253	0.082	0.301	0.096	0.170
Flexural	164.77	154.98	88.13	130.63	431.95	465.35
modulus (MPa)	(121.11–188.36)	(146.07–163.29)	(73.99–104.70)	(95.57–173.87)	(350.62–564.20)	(449.74–565.19)
P value		0.443	0.068	0.115	**0.002**	**<0.001**
Femoral geometry						
FHA (mm^2)*	1.19 ± 0.5	1.21 ± 0.13	1.24 ± 0.10	1.20 ± 0.11	1.24 ± 0.09	1.27 ± 0.04
P value		1.000	1.000	1.000	1.000	1.000
NSA (°)*	130.32 ± 5.24	136.75 ± 6.60	133.00 ± 2.65	136.17 ± 3.33	134.20 ± 4.44	130.40 ± 4.93
P value		0.400	1.000	1.000	1.000	1.000
Cartilage parameters						
CECT (HU)	2451.36	3854.90	3989.71	3867.51	3911.63	3814.69
	(2304.5–2596.6)	(3757.5–4007.5)	(3948.7–4030.3)	(3782.6–3962.8)	(3874.2–4006.0)	(3667.1–4277.4)
P value		**0.007**	0.157	0.288	0.341	0.296
Cartilage volume (mm^3)	0.37 (0.35–0.41)	0.27 (0.25–0.28)	0.11 (0.10–0.12)	0.18 (0.18–0.19)	0.18 (0.18–0.21)	0.19 (0.19–0.22)
P value		0.055	**0.012**	0.161	0.145	0.077

P values represent statistical significance of differences among groups; multiple comparisons are included in text. HU, Hounsfield units.
*These measurements are reported as mean and SD.

No significant differences were observed in MinDens values between 8mWT and HGPS-Ctrl mice. Animals treated with lonafarnib monotherapy (P1L) had a 14% decrease ($P = 0.106$) in MinDens when compared to HGPS-Ctrl mice, while the remaining treatment arms showed no changes in MinDens when compared to HGPS mice without treatment. The 2mWT mice had the lowest cortical MinDens values among all groups, which increased by almost 19% with age in 8mWT mice ($P < 0.001$).

There were no significant differences in cortical indices between male and female mice overall or within each treatment group (*P* values >0.05).

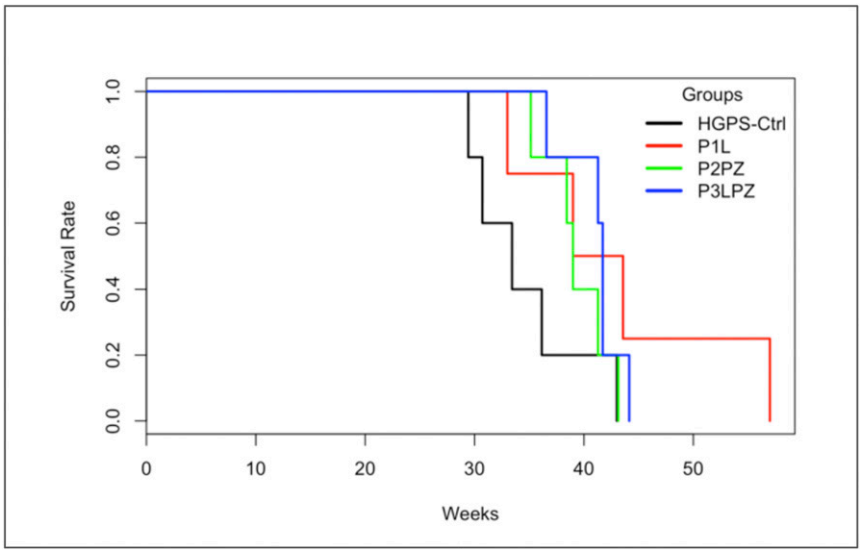

Fig. 1. Kaplan–Meier curves and estimates of survival for all HGPS mice.

Table 3. Age at death in weeks for HGPS mice

Group	*n*	%	Age at death (mean ± SD)	*P* value
HGPS-Ctrl	5	26.3	34.5 ± 5.4	—
Male	2		36.9 ± 8.7	0.455
Female	3		33.0 ± 3.4	
P1L	4	21.1	43.1 ± 10.2	0.113*
Male	2		50.3 ± 9.5	0.090
Female	2		36.0 ± 4.2	
P2PZ	5	26.3	39.4 ± 3.0	0.206*
Male	2		40.1 ± 1.6	0.946
Female	3		38.9 ± 4.0	
P3LPZ	5	26.3	41.1 ± 2.8	0.124*
Male	3		42.4 ± 1.5	0.397
Female	2		39.1 ± 3.6	

**P* values that represent the comparison of longevity of each treatment arm independently vs. HGPS-Ctrl mice.

Trabecular Bone Material Properties: Volume Fraction; Tb.N, Tb.Th, and Tb.Sp.; SMI, MinDens, ConnD, and DA. There were no significant changes observed in trabecular indices between 8mWT mice and HGPS-Ctrl mice. Combined treatment groups (P2PZ and P3LPZ) had an 81% increase in BV/TV values when compared to HGPS-Ctrl mice ($P = 0.004$ and $P < 0.001$, respectively). Regarding trabecular microstructural indices, P3LPZ had a 108% ($P = 0.014$) increase in Tb.N and a 53% decrease in Tb.Sp ($P = 0.017$) when compared to HGPS-Ctrl mice. No significant changes were observed in Tb.Th values between HGPS-Ctrl mice and the HGPS-treated mice. In terms of SMI values, P2PZ (SMI = 1.87) and P3LPZ mice (SMI = 1.74) had significant decreases in their SMI (42% and 46%, respectively; $P < 0.004$ and < 0.001, respectively) when compared to HGPS-Ctrl mice (SMI = 3.24). No significant changes were observed in ConnD, MinDens, and DA between HGPS-Ctrl and HGPS-treated mice.

BV/TV was significantly lower ($P = 0.005$) in 8mWT when compared to younger 2mWT mice. While Tb.N decreased by 60% with age from 2mWT to 8mWT mice ($P < 0.001$), Tb.Th and Tb.Sp values increased 50% and 145%, respectively ($P < 0.001$). In addition, 8mWT mice had a 92% decrease in ConnD ($P < 0.002$), a 41% decrease in DA ($P < 0.001$), and a 29% increase in SMI (SMI = 2.61; $P = 0.004$) when compared to 2mWT mice as observed in Table 1.

Significant differences were observed between male and female mice in Tb.N ($P = 0.02$), Tb.Th ($P = 0.009$), and Tb.Sp ($P = 0.003$) when considering all males and females combined for each trabecular parameter analysis. More specifically, female mice exhibited a lower Tb.N, and higher Tb.Th and Tb.Sp values.

CTRA: Axial, Bending, and Torsional Rigidities. HGPS-Ctrl mice showed a decreasing trend in EA (43%), EI (57%), and torsional (GJ; 56%) rigidities when compared to 8mWT mice as observed in Fig. 2. In P2PZ-treated mice, EI and GJ rigidity values increased 145% ($P = 0.034$) and 143% ($P = 0.032$), respectively, when compared to HGPS-Ctrl mice. Although EA, EI, and GJ values showed an increasing trend in the P3LPZ group, there was no significant difference when compared to HGPS-Ctrl mice. EA, EI, and GJ rigidities significantly increased with aging (from 2mWT to 8mWT), as shown in Fig. 2 ($P < 0.001$).

No significant differences were observed in rigidity values between male and female mice overall or within each treatment group ($P > 0.05$).

Mechanical Testing: Yield Stress, Ultimate Stress, and Flexural Modulus. Yield stress and ultimate stress values exhibited increasing trends (37% and 35%, respectively) in HGPS-Ctrl when compared to 8mWT mice, as observed in Table 2. Regarding the flexural modulus values, HGPS-Ctrl mice had a decreasing trend (43%, $P = 0.068$) when compared to the age-matched WT mice (8mWT group).

Multiple drug combinations had no effect on yield stress and ultimate stress values when compared to HGPS-Ctrl mice. However, flexural modulus values significantly increased 4.9 to 5.3 times in the P2PZ- and P3LPZ-treated mice when compared to the HGPS-Ctrl mice ($P = 0.002$ and $P < 0.001$, respectively).

Yield stress, ultimate stress and flexural modulus values had a decreasing tendency in older WT mice (4.4%, 4.3%, and 5.9%, respectively) when compared to the healthy young mice (2mWT).

There were no significant differences in mechanical testing measurements between male and female mice overall or within each treatment group ($P > 0.05$).

Femoral Head Geometry: FHA and NSA. There were no geometrical differences in the femoral head morphology of the HGPS-Ctrl mice when compared to age-matched WT mice (8mWT), as observed in Table 2. Moreover, no treatment combinations exhibited significant differences in both FHA and NSA when compared to

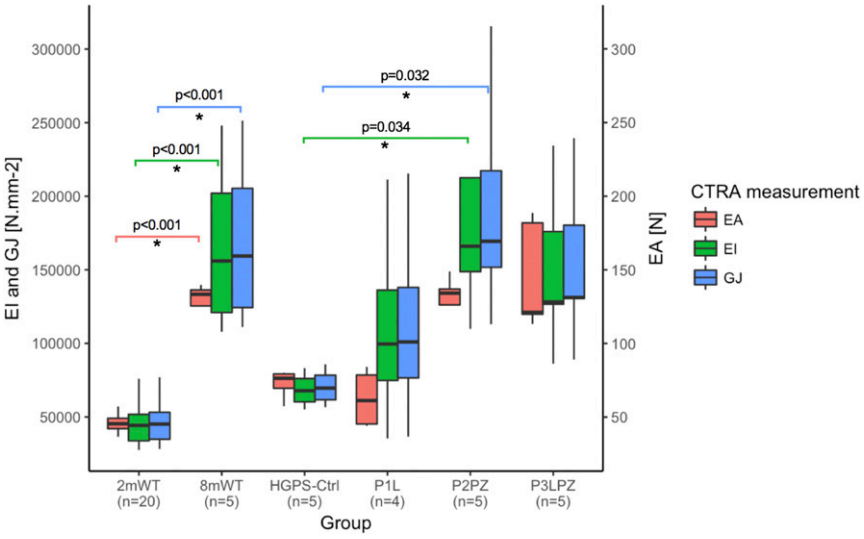

Fig. 2. Computed tomography rigidity analysis. Only significant (*) *P* values are displayed.

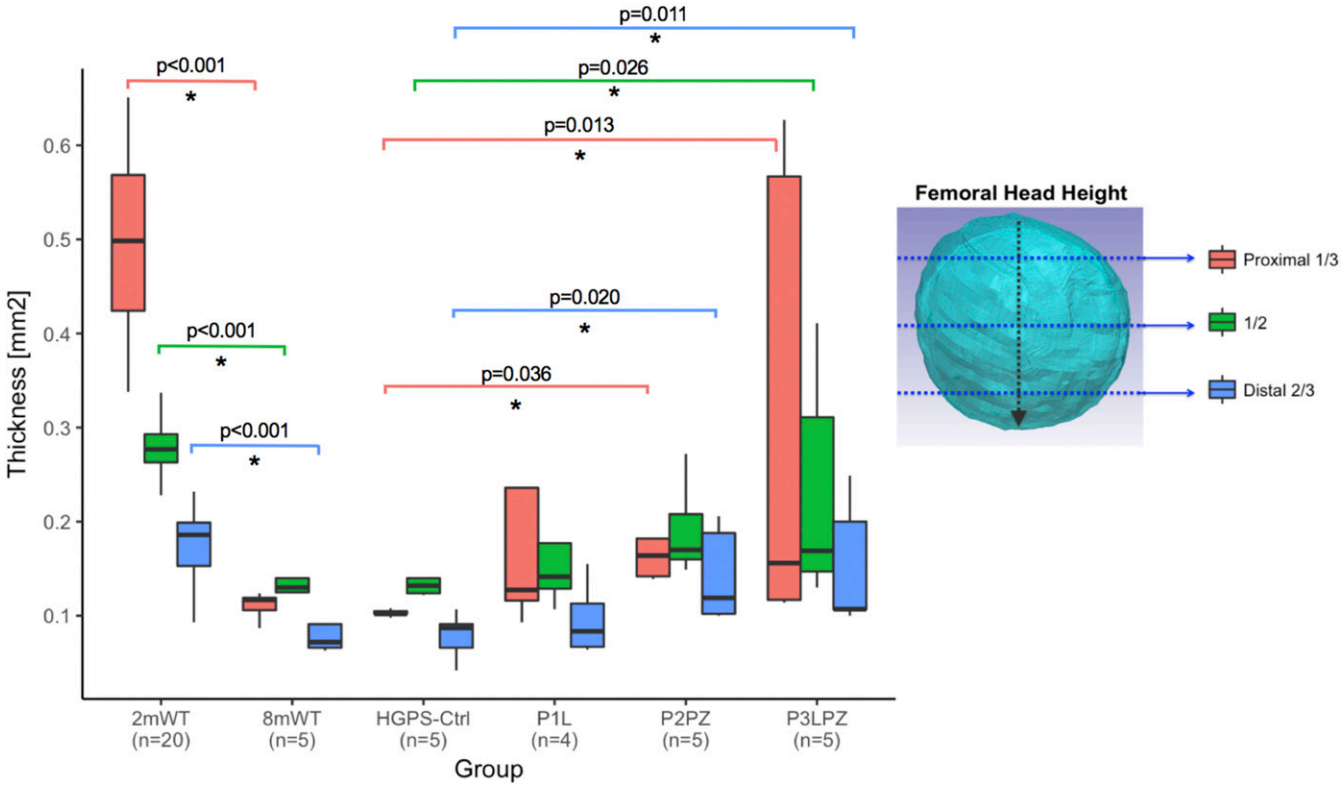

Fig. 3. Cartilage thickness (millimeters) at the proximal one-third, one-half, and two-thirds distal of the femoral head.

HGPS-Ctrl mice. In addition, no relevant changes were observed in FHA or NSA between young healthy mice and 8mWT mice.

There were no differences in measurements between male and female mice within each treatment group ($P > 0.05$).

Cartilage Structure and Biomechanical Composition: Cartilage Thickness, AGEs, GAG Content, and Cartilage Volume. Cartilage thickness assessed at the proximal third of the femoral head height in HGPS-Ctrl mice was not significantly different from 8mWT mice. Combined treatments (P2PZ and P3LPZ) exhibited higher cartilage thickness values when compared to HGPS-Ctrl mice ($P = 0.036$ and $P = 0.013$, respectively). However, no significant differences were observed in mice treated with lonafarnib alone (P1L) when compared to HGPS-Ctrl mice.

Cartilage thickness at the proximal third of the femoral head height significantly decreased with age (78%) when compared to 2mWT mice ($P < 0.001$), as observed in Fig. 3. Changes in cartilage thickness observed at the middle and at the distal thirds mirrored the differences described at the proximal third of the femoral head height above.

AGEs have been described to increase oxidative stress and inflammation in different tissues, such as heart, lung, skeletal muscle, bone, and brain. These macromolecules have been described to accumulate with age in multiple organ systems and cause

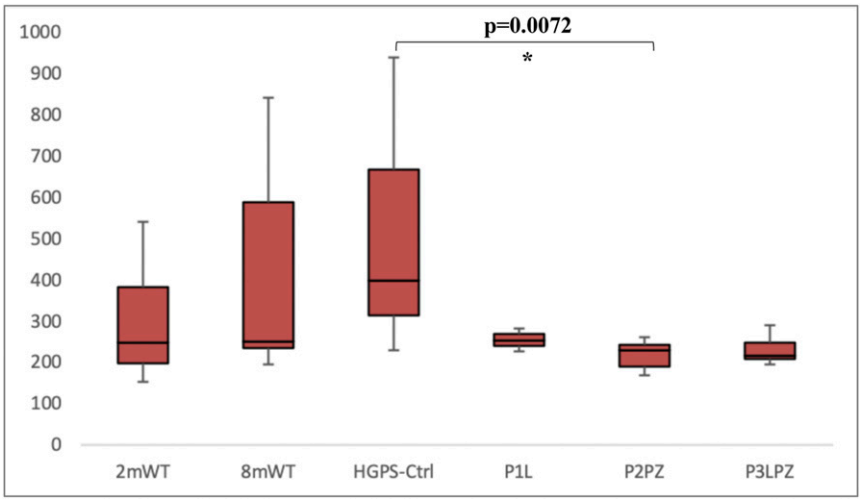

Fig. 4. AGE content in the femoral diaphysis. Only significant (*) *P* values are displayed.

AGE-associated damage by creating covalent cross-links with extra-cellular matrix and vascular basement membrane proteins (45). We observed that there were no significant differences in the amount of AGEs in the femoral diaphysis between HGPS-Ctrl and 8mWT mice. Mice that received a combined treatment with pravastatin and zoledronic acid (P2PZ) exhibited a lower quantity of AGEs when compared to HGPS-Ctrl mice ($P = 0.0072$; means = 219.7 and 523.2 ng quinine per milligram collagen, respectively). No significant differences were observed between HGPS-Ctrl mice and the remaining treatment arms. However, there tended to be fewer AGE accumulation in treated mice with P1L (mean = 255.4 ng quinine per milligram collagen) and P3LPZ (mean = 233.3 ng quinine per milligram collagen) compared to HGPS-Ctrl mice as shown in Fig. 4. In addition, no relevant changes were observed between young healthy and 8mWT mice, or between male and female mice.

GAG content assessed by the CECT attenuation of the femoral head cartilage (inversely related to overall cartilage GAG content) exhibited no differences between 8mWT and HGPS-Ctrl mice ($P = 0.157$), as observed in Table 2. In addition, no differences in GAG content were observed between each treatment arm and HGPS-Ctrl mice. CECT attenuation significantly increased with age as observed in the age-matched WT mice (8mWT) when compared to 2-mo-old WT mice ($P = 0.007$), indicating that 8mWT mice had a lower overall cartilage GAG content.

As previously described, 3D reconstructions of the femoral head articular cartilage were performed by contouring three anatomical planes: Sagittal, coronal, and axial sections. The HGPS and age-matched WT controls (8mWT) notably exhibited cartilage degradation evidenced by the lack of tissue covering some articular surface areas (Fig. 5). Further volumetric evaluations indicated a significant decrease in cartilage volume in HGPS mice (0.11 mm^3) when compared 8mWT (0.27 mm^3, $P = 0.012$). However, no significant differences in cartilage volume were observed between each treatment arm and HGPS-Ctrl mice. Cartilage volume shows a decreasing trend with older age (27%) when comparing 8mWT with 2mWT mice (0.37 mm^3, $P = 0.055$).

There were no significant differences in cartilage parameters reported above between male and female mice overall or within each treatment group ($P > 0.05$).

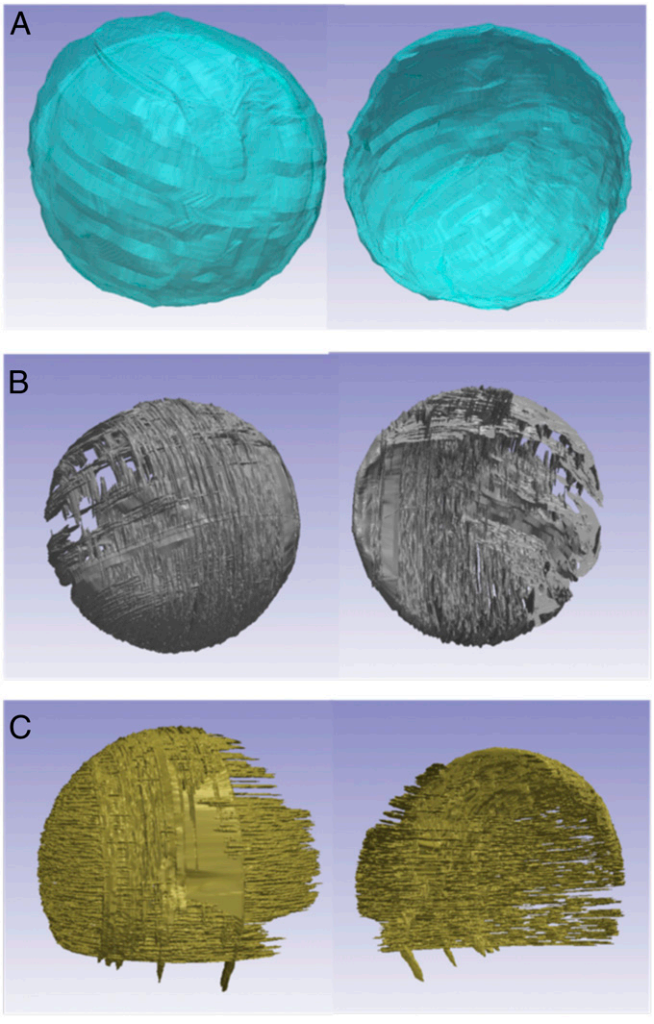

Fig. 5. Three-dimensional reconstruction of the articular and endochondral surfaces of the femoral head. (*A*) 2mWT, (*B*) 8mWT, (*C*) HGPS-Ctrl mice.

Discussion

Bone Geometry, Microstructure, and Mechanical Properties. Our results indicate that the HGPS-Ctrl mice show decreased Ct.Th in their femurs, while maintaining the same bone MinDens when compared to 8mWT mice. Other models of HGPS, such as the Zpmste24$^{-/-}$, also report decreased Ct.Th in the tibias of the mutant mice, which can be rescued by the addition of statins and bisphosphonates to the treatment regimen (46). The mice receiving lonafarnib monotherapy had decreasing trends in Ct.Th (15%) and cortical MinDens (14%) when compared to the HGPS-Ctrl mice, but no significant differences were noted. As expected, addition of pravastatin and zoledronic acid significantly improved Ct.Th values and achieved the highest values in all treatment groups. As reported in previous studies in humans (1, 2), we did not find any differences in cortical bone MinDens in the HGPS-Ctrl mouse model when compared to healthy age-matched mice (8mWT).

Trabecular bone abnormalities observed in the HGPS-Ctrl group were not significantly different from 8mWT mice. Furthermore, trabecular indices remained unchanged in mice treated with lonafarnib when compared to HGPS-Ctrl animals. As previously reported in clinical trials with HGPS patients, adding pravastatin and zoledronic acid exerts an additional benefit in cancellous and cortical bone parameters (24, 46). In the homozygous G608G mice, cancellous bone improvements were observed in the combined treatment groups. This was reflected by increased BV/TV and Tb.N, and decreased SMI and Tb.Sp. The addition of statins and bisphosphonates brings trabecular parameters closer to that of young healthy WT mice (2mWT).

Trabecular differences observed between male and female mice resemble those reported in the literature (47, 48) and include lower Tb.N, and higher Tb.Th and Tb.Sp values in the female population as a whole. Glatt et al. (48) report that declines in vertebral and distal femoral trabecular bone volume throughout age are more pronounced in female than male C57BL/6J (WT) mice. More specifically, Tb.N was reported to be lower in the vertebrae and distal femur of female mice when compared to male mice at all ages (48). Robertson et al. (47) also report gender differences in bone microstructural parameters. The trabecular microarchitecture in all studied regions exhibited better morphometric indices in male mice when compared to their female littermates. Lower Tb.N and higher Tb.Sp were observed in WT female mice when compared to WT male mice (47). These observed changes in trabecular bone between genders can be potentially explained by the effect of gender-specific hormones on bone metabolism. Nonetheless, the structural differences observed in this study had no impact on rigidity or biomechanical properties.

It has been previously described that the deterioration of trabecular bone due to aging and disease is characterized by a conversion from plate to rod elements (49). The SMI allows quantifying of the characteristic form of a 3D-described structure in terms of the amount of plates and rods composing the trabecular structure of interest. More specifically, for an ideal plate and rod structure, the corresponding SMI assigned values are 0 and 3, respectively. Interestingly, the higher SMI in trabecular bone of HGPS-Ctrl mice (SMI = 3.2) suggests a more predominant rod-like structure (49) than their age-matched (SMI = 2.6) healthy WT animals (8mWT). Therefore, the trabecular geometry of the HGPS-Ctrl mouse femurs may resemble that of an aged bone. CTRA was used to assess the rigidity of bones, or the capacity of bones to resist different types of loads. Rigidity analyses showed similar results to bone mechanical properties as measured by mechanical testing of femurs. The HGPS-Ctrl and lonafarnib (P1L) mice showed the lowest rigidities and flexural modulus (intrinsic stiffness) values. There were no protective effects of lonafarnib on the HGPS-Ctrl mice for these indices. Interestingly, rigidity indices were higher in both combined treatment groups (Fig. 2), with no significant differences between them. Mice treated with the two-drug combination (pravastatin and zoledronic acid) exhibited a significant increase in EI (145%) and GJ (143%) rigidities ($P = 0.03$). Moreover, mice treated with the three-drug regimen (pravastatin, zoledronic acid, and lonafarnib) exhibited an increasing trend in all three indices (EA, EI, and GJ rigidities) when compared to HGPS-Ctrl mice, but with overall smaller median rigidity values when compared to P2PZ. The observed increased rigidities observed in the P2PZ group are comparable to the range of rigidity improvement observed in a clinical trial with HGPS patients (24) and can be explained by the bone-protective effects due to the addition of both pravastatin and zoledronic acid to the HGPS mice treatment regimen. These medications target bone resorption and also have anabolic effects on bone (50–52). Unlike HGPS patients in the clinical trial by Gordon et al. (24), mentioned above, no protective effects on bone rigidity indices were observed with the use of lonafaranib alone.

A clinical trial including 26 children with HGPS (ages 3.1 to 16.2 y) concluded that HGPS primarily affects the structural geometry rather than the bone material properties, which is suggestive of a skeletal dysplasia (1, 2, 53). While vBMD was not different in children with HGPS when compared to age-matched healthy patients, CTRA results indicated that children with HGPS had 40% lower EA, and 66% lower EI, and GJ rigidities when compared to healthy controls. In our animal study, similar reductions were observed. When compared to 8mWT mice, average HGPS mouse EA was 43% lower, and average EI and GJ were 57% lower. Furthermore, we did not encounter any differences in BMD measurements comparing HGPS and age-matched WT mice.

Overall, our results show that lonafarnib monotherapy did not exhibit a significantly improved bone phenotype in the previously mentioned bone microstructural parameters. However, treatment with lonafarnib alone did show improving trends in some bone indices (decreasing trends in Ct.Th and cortical MinDens when compared to HGPS-Ctrl mice). In addition, trabecular indices and bone rigidity parameters remained unchanged in mice treated with lonafarnib monotherapy when compared to HGPS-Ctrl animals. As previously reported in clinical trials with HGPS patients (24), the addition and synergistic effect of pravastatin and zoledronic acid showed significant bone phenotype improvements in HGPS mice.

The homozygous G608G mouse model exhibits an altered bone phenotype in the cortical structural properties as a consequence of the disease. These cortical bone alterations, in conjunction with an altered rigidity and ultimate stress profile, could provide a possible explanation for the musculoskeletal changes found in patients with HGPS. By having lower rigidity values and lower Ct.Th, bones could be at increased risk for bending and deformation, which could result in the characteristic skeletal dysplasia of HGPS, such as coxa valga (NSA above 135°). In contrast to previous clinical studies that describe an altered hip geometry of patients with HGPS (1, 53), coxa valga (NSA), and coxa magna (asymmetrical circumferential enlargement of the FHA) were not observed in our HGPS mouse femurs. However, the decreased physical activity of animals under laboratory conditions and the differences in weight-bearing status between humans (bipeds) and animals (quadrupeds) (54) could potentially explain the absence of morphological changes in the femurs of the HGPS mice in our study.

Although HGPS mice exhibited a decreasing trend of rigidity profiles and flexural modulus (tendency to resist bending), P2PZ- and P3LPZ-treated mouse femurs had higher rigidity values and a flexural modulus 4.9 and 5.3 times higher, respectively. However, bisphosphonates alone would not be responsible for the increase in rigidity and mechanical properties present in these treatment arms (46). A recent metaanalysis conducted in 2016 concluded that statin use seems to be associated with higher BMD values and could be a potential treatment to improve bone health (55). This might also account for the increased rigidity and mechanical properties of the femoral cortical bone in the combined treatment arms.

Cartilage Structure and Biomechanical Composition. Musculoskeletal abnormalities reported in animal models of progeroid laminopathies mainly focus on describing the bone phenotype of HGPS. Commonly reported bone disorders include generalized osteoporosis, spontaneous fractures, bone mineralization defects, joint contractures, and dysplastic long bones. However, there is insufficient literature on whether HGPS may cause any potential premature cartilage disease.

In this study, we performed direct and indirect assessments of cartilage health in the articular cartilage of the femoral head from G608G homozygous mice. Indirect measurements included measuring GAG and AGEs, which give information related to the cartilage biochemical composition. GAGs are specifically important markers, as they can change early in the course of a musculoskeletal disease such as osteoarthritis (OA). In addition, quantitative measurements of thickness (millimeter, mm) and volume (cubic millimeter, mm^3) aimed to assess macroscopic changes in the structure of the cartilage itself.

Mean attenuation values assessed with CECT were the lowest in the young WT mice group, meaning that GAG content was significantly higher in this group when compared to the other five experimental arms. In contrast, HGPS mice exhibited the highest mean attenuation values, indicating that HGPS mice had the lowest cartilage GAG content overall. However, treatment arms did not exhibit a significant improvement when compared to HGPS-Ctrl mice (Table 2). Depletion of GAG content in the cartilage increases tissue permeability, which in turn decreases interstitial fluid load support, thereby softening the cartilage and increasing its coefficient of friction. It is the early loss of GAG that is currently described as one of the first manifestations of cartilage degradation. In this way, cartilage resistance to compressive loads is adversely affected, and cartilage thickness and volume are compromised at a later stage.

Cartilage thickness from HGPS and 8mWT mice were significantly decreased when compared to young healthy WT mice in all cross-sections ($P < 0.001$). In addition, combined treatment groups with statins and bisphosphonates showed increased cartilage thickness values in all cross-sections of HGPS mice (Fig. 3).

After a slice-by-slice contouring process in all directions (axial, sagittal, and coronal) of a high-resolution CT scan (6 μm), a 3D reconstruction was performed for direct visualization of the cartilage articular and endochondral surfaces. Macroscopic cartilage degradation was observed in the HGPS-Ctrl mice in areas devoid

of cartilage tissue, as shown in Fig. 5. Moreover, per software calculation, we obtained precise volumetric measurements of the previously contoured regions. Cartilage degradation observed in Fig. 5 correlates with the lower cartilage volumes found in 8mWT and HGPS-Ctrl mice.

As previously mentioned, there is limited data available regarding animal models whose primary focus is on cartilage structure and composition in HGPS models. For example, a study performed in 20-wk-old progeroid mice demonstrated intervertebral disk degeneration (56). Among other degenerative changes, the discs showed loss of disk height and premature loss of matrix proteoglycans, which is comparable to the changes observed in our HGPS and 8mWT mice. Another study, focusing on cartilage biochemical parameters in HGPS, describes the altered expression of aggrecan in skin fibroblasts lines from HGPS patients, one of the most abundant proteoglycans in the cartilage ECM (57). These cells exhibited up-regulation in the expression of aggrecan when compared to their controls. However, it is still unclear whether similar transcriptional changes occur in human chondrocytes. Previous clinical studies rely strongly on X-ray imaging for the assessment of arthritis signs. For example, in a study performed in hips, ankles, knees, and wrists from 21 children with HGPS, no radiographic evidence of arthritis was observed (53).

Our cartilage findings are in line with recent in vitro studies that focus on the molecular background of the HGPS documented abnormalities in the musculoskeletal system. These studies link the accumulation of progerin with altered cellular mechanisms that can explain the phenotype of the disease present in bone and cartilage. Altered signaling pathways described in HGPS that are relevant to the musculoskeletal homeostasis include the Wnt/β catenin pathway and the mechanotransduction pathway.

The Wnt/β-catenin pathway has been shown to have decreased activity in HGPS cells (58, 59). For example, fibroblasts from the *Lmna* Δ9 progeria mouse model and hair follicle stem cells in *Zmpste24*$^{-/-}$ mice have shown reduced Wnt/β-catenin signaling (16, 60). This alteration leads to mesenchymal stem cell dysfunction (7), as well as an altered expression of ECM genes with specific roles in skeleton and cartilage development (16, 58, 59).

Mechanotransduction describes the adaptive response by which cells respond to changes in mechanical loads exerted by their environment (61). WT cells respond to physical stress by activating specific gene-expression programs that include up-regulation and redistribution of type A lamins (62, 63). Accumulation of progerin in HGPS cells leads to thickening and increased stiffness of the lamina, which results in stiffer and less compliant nuclei (61, 63). HGPS fibroblasts have been shown to have increased mechanosensitivity and react to mechanical strain with apoptosis/necrosis and impaired strain-induced proliferation response (61, 64, 65). This abnormal adaptive response in HGPS cells places tissues exposed to high shear stress—such as vasculature, bone, and joints—to be more susceptible to damage (63).

Our cartilage results outline interesting degenerative changes in the HGPS articular cartilage, which resemble those observed in the age-matched WT controls. Currently, it remains unclear whether HGPS causes premature cartilage abnormalities that resemble articular degeneration, characteristic of elderly individuals. OA is a chronic debilitating disease that degrades articular cartilage and is characterized by the early loss of matrix GAGs. OA is one of the most common causes of chronic disability and pain in the elderly population, and accelerated aging animal models could offer a unique opportunity for the study of degenerative joint diseases. Therefore, further studies with HGPS G608G mice at different growth stages would be useful to determine whether HGPS mice have comparable disease to senile WT rodents, and could be of use to assess new therapeutic approaches for highly prevalent debilitating joint diseases, such as OA.

Limitations. The ability to obtain and manipulate BAC clones with genomic DNA spanning hundreds of kilobases is highly advantageous for transgenic applications, given that most BAC clones encode the complete Open Reading Frame and most regulatory sequences, which recapitulate the regulation of endogenous genes much better than shorter transgenes (66). Thus, BACs provide a direct accurate, endogenous-like expression of the disease-causing proteins of interest. In this large-scale addition of introns and exons of a human gene, the mouse environment may cause unexpected phenotypes. Currently, this is unpredictable and must be assessed on a case-by-case basis but does not preclude working with such animals (67).

A major limitation of the present study is that the BAC used (172 kb: vector and insert) also carries other genes (*UBQLN4*, *MAPBPIP*, *RAB25*, and *MEX3A*) in addition to *LMNA*, which could affect the disease phenotype. Although we do not include supplemental data regarding the potential overexpression of these genes in this homozygous mouse model, these concerns were previously addressed the in the heterozygous (p.G608G/+) HGPS mouse model described by Varga et al. (30). To assess the potential effect of other genes carried in the BAC (*UBQLN4*, *MAPBPIP*, and *RAB25*) in addition to *LMNA*, Varga et al. created control animals carrying a WT human *LMNA* BAC. Interestingly, they observed that phenotype of the WT transgenics was essentially normal, except for possibly very mild medial arterial changes in animals of advanced age (30).

The mutant form of lamin A (progerin) responsible for the premature aging disease in HGPS acts as a dominant-negative protein (4, 68–71). In addition, the permanently farnesylated state of progerin allows it to exert its dominant-negative effects and cause the devastating effect on cellular function, accelerating the senescence of cells that express it (63, 72–74). Thus, as disease in HGPS is produced by a dominant-negative mechanism; it is the effect of progerin, not the diminution of lamin A, that causes the disease phenotype (23). Although human *UBQLN4*, *MAPBPIP*, *RAB25*, and *MEX3A* genes can be expressed from the BAC in the G608G homozygous mouse model, the homozygous mice develop and progress without neoplasia, aggressive tumors, or T cell deficiencies characteristic of overexpression of these genes (75–82). The most important feature of this HGPS mouse model is the overexpression of the dominant-negative human progerin protein.

Another limitation of this study is the small sample size ($n = 5$) in each transgenic mouse group and the additional stratification by gender. The low sample size may have yielded high variability in some measurements that could account for the lack of differences in some bone material and mechanical properties, cartilage structural and biochemical parameters, and overall survival. Survival rates were not improved in HGPS-treated mice in this animal model, but a study with bigger sample size would be able to properly address the impact of the combined treatment regimens in the longevity of G608G mice. Therefore, an increased sample size would be ideal to determine the differences in outcomes between groups more definitively. Moreover, our results describe bone and cartilage changes in 2-mo-old (young WT) and older age-matched WT animals, but changes during growth could not be assessed. Furthermore, given that we have investigated an animal model, the external validity of our results may be limited. Therefore, interpretation of results and their applicability to humans must be considered with caution. This is of particular importance given the differences in weight-bearing status between mice and humans, and how this could potentially affect bone metabolism.

Conclusions

The changes demonstrated in the cortical bone structure, rigidity, stiffness, and flexural modulus of the HGPS G608G mouse model may increase the risk for bending and deformation of bones, which could result in the skeletal dysplasia characteristic of HGPS patients. Differences in the distribution of weight-bearing status

between humans and mice may provide an explanation for the absence of morphological changes in this animal model, which may serve as a progeria mouse model. Even though lonafarnib alone did not improve any bone or cartilage outcomes, it did not counter the positive effects of combined treatment with statins or bisphosphonates. This was mostly reflected in the improvement of trabecular bone indices observed in the P3LPZ group in Table 1, such as increased BV/TV ($P < 0.001$) and Tb. N ($P = 0.014$), decreased SMI ($P < 0.001$) and Tb.Sp ($P = 0.017$), and increased flexural modulus ($P < 0.001$) when compared to HGPS-Ctrl mice. Other trends toward improvement in the P3LPZ group were evident in ConnD ($P = 0.051$) and EA-EI-GJ rigidities. Given the lack of changes in bone or cartilage structure with lonafarnib and the clear benefits reported in survival rates in animal and clinical studies (23, 25, 46), it should always be considered as a treatment option for the disease.

Cartilage abnormalities seen in this HGPS model resemble those observed in the age-matched WT controls. Further studies at different growth stages would allow researchers to understand cartilage health and structure in order to determine whether cartilage degeneration in G608G progeria mice is attributable to premature aging of the tissue itself or due to a developmental alteration. In addition, this raises the question of whether HGPS G608G mice could be used as an accurate animal model that resembles degenerative joint disease in the elderly population, and serve for further research approaches toward the early detection, management and development of novel therapeutics for OA.

ACKNOWLEDGMENTS. The authors thank Dr. Leslie Gordon for her help with the manuscript, and Drs. Dan Ellis, Rachel Stewart, and Benjamin Cooper for their contribution on bone and cartilage assessment. This work was supported by National Institutes of Health Loan Repayment Program AR055885 (to A.N.), and The Progeria Research Foundation.

1. M. A. Merideth *et al*., Phenotype and course of Hutchinson-Gilford progeria syndrome. *N. Engl. J. Med.* **358**, 592–604 (2008).
2. C. M. Gordon *et al*., Hutchinson-Gilford progeria is a skeletal dysplasia. *J. Bone Miner. Res.* **26**, 1670–1679 (2011).
3. A. De Sandre-Giovannoli *et al*., Lamin a truncation in Hutchinson-Gilford progeria. *Science* **300**, 2055 (2003).
4. M. Eriksson *et al*., Recurrent de novo point mutations in lamin A cause Hutchinson-Gilford progeria syndrome. *Nature* **423**, 293–298 (2003).
5. S. M. Kang, M. H. Yoon, B. J. Park, Laminopathies; Mutations on single gene and various human genetic diseases. *BMB Rep.* **51**, 327–337 (2018).
6. C. Gargiuli *et al*., Lamins and bone disorders: Current understanding and perspectives. *Oncotarget* **9**, 22817–22831 (2018).
7. K. Harhouri *et al*., An overview of treatment strategies for Hutchinson-Gilford progeria syndrome. *Nucleus* **9**, 246–257 (2018).
8. J. L. Broers, F. C. Ramaekers, G. Bonne, R. B. Yaou, C. J. Hutchison, Nuclear lamins: Laminopathies and their role in premature ageing. *Physiol. Rev.* **86**, 967–1008 (2006).
9. T. Dechat, K. Gesson, R. Foisner, Lamina-independent lamins in the nuclear interior serve important functions. *Cold Spring Harb. Symp. Quant. Biol.* **75**, 533–543 (2010).
10. K. Gesson, S. Vidak, R. Foisner, Lamina-associated polypeptide (LAP)2α and nucleoplasmic lamins in adult stem cell regulation and disease. *Semin. Cell Dev. Biol.* **29**, 116–124 (2014).
11. V. Kochin *et al*., Interphase phosphorylation of lamin A. *J. Cell Sci.* **127**, 2683–2696 (2014).
12. N. Naetar, S. Ferraioli, R. Foisner, Lamins in the nuclear interior—Life outside the lamina. *J. Cell Sci.* **130**, 2087–2096 (2017).
13. G. Krohne, I. Waizenegger, T. H. Höger, The conserved carboxy-terminal cysteine of nuclear lamins is essential for lamin association with the nuclear envelope. *J. Cell Biol.* **109**, 2003–2011 (1989).
14. A. E. Rusiñol, M. S. Sinensky, Farnesylated lamins, progeroid syndromes and farnesyl transferase inhibitors. *J. Cell Sci.* **119**, 3265–3272 (2006).
15. T. Dechat *et al*., Alterations in mitosis and cell cycle progression caused by a mutant lamin A known to accelerate human aging. *Proc. Natl. Acad. Sci. U.S.A.* **104**, 4955–4960 (2007).
16. L. Hernandez *et al*., Functional coupling between the extracellular matrix and nuclear lamina by Wnt signaling in progeria. *Dev. Cell* **19**, 413–425 (2010).
17. R. D. Goldman *et al*., Accumulation of mutant lamin A causes progressive changes in nuclear architecture in Hutchinson-Gilford progeria syndrome. *Proc. Natl. Acad. Sci. U.S.A.* **101**, 8963–8968 (2004).
18. A. D. Basso, P. Kirschmeier, W. R. Bishop, Lipid posttranslational modifications. Farnesyl transferase inhibitors. *J. Lipid Res.* **47**, 15–31 (2006).
19. L. B. Gordon *et al*., Clinical trial of a farnesyltransferase inhibitor in children with Hutchinson-Gilford progeria syndrome. *Proc. Natl. Acad. Sci. U.S.A.* **109**, 16666–16671 (2012).
20. B. C. Capell *et al*., A farnesyltransferase inhibitor prevents both the onset and late progression of cardiovascular disease in a progeria mouse model. *Proc. Natl. Acad. Sci. U.S.A.* **105**, 15902–15907 (2008).
21. S. H. Yang *et al*., A farnesyltransferase inhibitor improves disease phenotypes in mice with a Hutchinson-Gilford progeria syndrome mutation. *J. Clin. Invest.* **116**, 2115–2121 (2006).
22. L. G. Fong *et al*., A protein farnesyltransferase inhibitor ameliorates disease in a mouse model of progeria. *Science* **311**, 1621–1623 (2006).
23. L. B. Gordon *et al*.; Progeria Clinical Trials Collaborative, Impact of farnesylation inhibitors on survival in Hutchinson-Gilford progeria syndrome. *Circulation* **130**, 27–34 (2014).
24. L. B. Gordon *et al*., Clinical trial of the protein farnesylation inhibitors lonafarnib, pravastatin, and zoledronic acid in children with Hutchinson-Gilford progeria syndrome. *Circulation* **134**, 114–125 (2016).
25. L. B. Gordon *et al*., Association of lonafarnib treatment vs no treatment with mortality rate in patients with Hutchinson-Gilford progeria syndrome. *JAMA* **319**, 1687–1695 (2018).
26. A. Jeong, K. F. Suazo, W. G. Wood, M. D. Distefano, L. Li, Isoprenoids and protein prenylation: Implications in the pathogenesis and therapeutic intervention of Alzheimer's disease. *Crit. Rev. Biochem. Mol. Biol.* **53**, 279–310 (2018).
27. T. Sullivan *et al*., Loss of A-type lamin expression compromises nuclear envelope integrity leading to muscular dystrophy. *J. Cell Biol.* **147**, 913–920 (1999).
28. L. C. Mounkes, S. Kozlov, L. Hernandez, T. Sullivan, C. L. Stewart, A progeroid syndrome in mice is caused by defects in A-type lamins. *Nature* **423**, 298–301 (2003).
29. D. McClintock *et al*., The mutant form of lamin A that causes Hutchinson-Gilford progeria is a biomarker of cellular aging in human skin. *PLoS One* **2**, e1269 (2007).
30. R. Varga *et al*., Progressive vascular smooth muscle cell defects in a mouse model of Hutchinson-Gilford progeria syndrome. *Proc. Natl. Acad. Sci. U.S.A.* **103**, 3250–3255 (2006).
31. M. O. Bergo *et al*., Zmpste24 deficiency in mice causes spontaneous bone fractures, muscle weakness, and a prelamin A processing defect. *Proc. Natl. Acad. Sci. U.S.A.* **99**, 13049–13054 (2002).
32. A. J. Dubose *et al*., Use of microarray hybrid capture and next-generation sequencing to identify the anatomy of a transgene. *Nucleic Acids Res.* **41**, e70 (2013).
33. Mouse Genome Informatics, C57BL/6-Tg(LMNA*G608G)HClns/J (2019). http://www.informatics.jax.org/allele/MGI:5441745#phenotypes. Accessed 10 June 2018.
34. J. C. Villa-Camacho, O. Iyoha-Bello, S. Behrouzi, B. D. Snyder, A. Nazarian, Computed tomography-based rigidity analysis: A review of the approach in preclinical and clinical studies. *Bonekey Rep.* **3**, 587 (2014).
35. M. Abramoff, P. Magalhães, S. J. Ram, Image Processing with ImageJ. *Biophoton. Int.* **11**, 36–42 (2004).
36. C. A. Schneider, W. S. Rasband, K. W. Eliceiri, NIH Image to ImageJ: 25 years of image analysis. *Nat. Methods* **9**, 671–675 (2012).
37. S. A. Qidwai, Z. K. Khattak, Treatment of femoral shaft fractures in children by intramedullary Kirschner wires. *J. Trauma* **48**, 256–259 (2000).
38. M. V. Rademakers, G. M. Kerkhoffs, I. N. Sierevelt, E. L. Raaymakers, R. K. Marti, Intra-articular fractures of the distal femur: A long-term follow-up study of surgically treated patients. *J. Orthop. Trauma* **18**, 213–219 (2004).
39. M. Maravic, C. Le Bihan, P. Landais, P. Fardellone, Incidence and cost of osteoporotic fractures in France during 2001. A methodological approach by the national hospital database. *Osteoporos. Int.* **16**, 1475–1480 (2005).
40. T. Scheerlinck, P. Krallis, P. Y. Descamps, D. Hardy, P. Delincé, The femoral supracondylar nail: Preliminary experience. *Acta Orthop. Belg.* **64**, 385–392 (1998).
41. J. P. Rao, M. Hambly, J. King, J. Benevenia, A comparative analysis of Ender's-rod and compression screw and side plate fixation of intertrochanteric fractures of the hip. *Clin. Orthop. Relat. Res.*, 125–131 (1990).
42. J. Gross, Studies on the formation of collagen. I. Properties and fractionation of neutral salt extracts of normal guinea pig connective tissue. *J. Exp. Med.* **107**, 247–263 (1958).
43. R Development Core Team, "R: A Language and Environment for Statistical Computing" (Version 3, R Foundation for Statistical Computing, Vienna, Austria, 2017).
44. RStudio Team, "RStudio: Integrated Development Environment for R" (Version 3.4, RStudio, Inc., Boston, MA, 2017).
45. R. D. Semba, E. J. Nicklett, L. Ferrucci, Does accumulation of advanced glycation end products contribute to the aging phenotype? *J. Gerontol. A Biol. Sci. Med. Sci.* **65**, 963–975 (2010).
46. I. Varela *et al*., Combined treatment with statins and aminobisphosphonates extends longevity in a mouse model of human premature aging. *Nat. Med.* **14**, 767–772 (2008).
47. G. Robertson *et al*., Alteration of femoral bone morphology and density in COX-2-/- mice. *Bone* **39**, 767–772 (2006).
48. V. Glatt, E. Canalis, L. Stadmeyer, M. L. Bouxsein, Age-related changes in trabecular architecture differ in female and male C57BL/6J mice. *J. Bone Miner. Res.* **22**, 1197–1207 (2007).
49. T. Hildebrand, P. Rüegsegger, Quantification of bone microarchitecture with the Structure Model Index. *Comput. Methods Biomech. Biomed. Engin.* **1**, 15–23 (1997).
50. U. Tatli, Y. Ustün, M. Kürkçü, M. E. Benlidayı, Effects of zoledronic acid on physiologic bone remodeling of condylar part of TMJ: A radiologic and histomorphometric examination in rabbits. *ScientificWorldJournal* **2014**, 649026 (2014).
51. S. B. Jadhav, G. K. Jain, Statins and osteoporosis: New role for old drugs. *J. Pharm. Pharmacol.* **58**, 3–18 (2006).
52. F. Ruan, Q. Zheng, J. Wang, Mechanisms of bone anabolism regulated by statins. *Biosci. Rep.* **32**, 511–519 (2012).

53. L. B. Gordon *et al*., Disease progression in Hutchinson-Gilford progeria syndrome: Impact on growth and development. *Pediatrics* **120**, 824–833 (2007).
54. C. M. Bagi, E. Berryman, M. R. Moalli, Comparative bone anatomy of commonly used laboratory animals: Implications for drug discovery. *Comp. Med.* **61**, 76–85 (2011).
55. J. W. Wang, C. Tang, B. R. Pan, Data analysis of low dose multislice helical CT scan in orbital trauma. *Int. J. Ophthalmol.* **5**, 366–369 (2012).
56. N. Vo *et al*., An overview of underlying causes and animal models for the study of age-related degenerative disorders of the spine and synovial joints. *J. Orthop. Res.* **31**, 831–837 (2013).
57. J. M. Lemire *et al*., Aggrecan expression is substantially and abnormally upregulated in Hutchinson-Gilford progeria syndrome dermal fibroblasts. *Mech. Ageing Dev.* **127**, 660–669 (2006).
58. T. F. Day, X. Guo, L. Garrett-Beal, Y. Yang, Wnt/beta-catenin signaling in mesenchymal progenitors controls osteoblast and chondrocyte differentiation during vertebrate skeletogenesis. *Dev. Cell* **8**, 739–750 (2005).
59. M. Chen *et al*., Inhibition of beta-catenin signaling causes defects in postnatal cartilage development. *J. Cell Sci.* **121**, 1455–1465 (2008).
60. J. Espada *et al*., Nuclear envelope defects cause stem cell dysfunction in premature-aging mice. *J. Cell Biol.* **181**, 27–35 (2008).
61. M. Prokocimer, R. Barkan, Y. Gruenbaum, Hutchinson-Gilford progeria syndrome through the lens of transcription. *Aging Cell* **12**, 533–543 (2013).
62. J. T. Philip, K. N. Dahl, Nuclear mechanotransduction: Response of the lamina to extracellular stress with implications in aging. *J. Biomech.* **41**, 3164–3170 (2008).
63. S. Vidak, R. Foisner, Molecular insights into the premature aging disease progeria. *Histochem. Cell Biol.* **145**, 401–417 (2016).
64. K. N. Dahl *et al*., Distinct structural and mechanical properties of the nuclear lamina in Hutchinson-Gilford progeria syndrome. *Proc. Natl. Acad. Sci. U.S.A.* **103**, 10271–10276 (2006).
65. V. L. Verstraeten, J. Y. Ji, K. S. Cummings, R. T. Lee, J. Lammerding, Increased mechanosensitivity and nuclear stiffness in Hutchinson-Gilford progeria cells: Effects of farnesyltransferase inhibitors. *Aging Cell* **7**, 383–393 (2008).
66. X. W. Yang, P. Model, N. Heintz, Homologous recombination based modification in Escherichia coli and germline transmission in transgenic mice of a bacterial artificial chromosome. *Nat. Biotechnol.* **15**, 859–865 (1997).
67. F. Zhu, R. R. Nair, E. M. C. Fisher, T. J. Cunningham, Humanising the mouse genome piece by piece. *Nat. Commun.* **10**, 1845 (2019).
68. P. Scaffidi, T. Misteli, Reversal of the cellular phenotype in the premature aging disease Hutchinson-Gilford progeria syndrome. *Nat. Med.* **11**, 440–445 (2005).
69. J. B. Kelley *et al*., The defective nuclear lamina in Hutchinson-Gilford progeria syndrome disrupts the nucleocytoplasmic Ran gradient and inhibits nuclear localization of Ubc9. *Mol. Cell. Biol.* **31**, 3378–3395 (2011).
70. D. Z. Bar *et al*., A novel somatic mutation achieves partial rescue in a child with Hutchinson-Gilford progeria syndrome. *J. Med. Genet.* **54**, 212–216 (2017).
71. B. Dorado *et al*., Generation and characterization of a novel knockin minipig model of Hutchinson-Gilford progeria syndrome. *Cell Discov.* **5**, 16 (2019).
72. L. B. Gordon, F. G. Rothman, C. López-Otín, T. Misteli, Progeria: A paradigm for translational medicine. *Cell* **156**, 400–407 (2014).
73. S. Ghosh, Z. Zhou, Genetics of aging, progeria and lamin disorders. *Curr. Opin. Genet. Dev.* **26**, 41–46 (2014).
74. V. Eisch, X. Lu, D. Gabriel, K. Djabali, Progerin impairs chromosome maintenance by depleting CENP-F from metaphase kinetochores in Hutchinson-Gilford progeria fibroblasts. *Oncotarget* **7**, 24700–24718 (2016).
75. R. D. Jachimowicz *et al*., UBQLN4 represses homologous recombination and is overexpressed in aggressive tumors. *Cell* **176**, 505–519.e22 (2019).
76. Y. Yu *et al*., UBQLN4 promotes progression of HCC via activating wnt-β-catenin pathway and is regulated by miR-370. *Cancer Cell Int.* **20**, 3 (2020).
77. G. Bohn *et al*., A novel human primary immunodeficiency syndrome caused by deficiency of the endosomal adaptor protein p14. *Nat. Med.* **13**, 38–45 (2007).
78. M. Łyszkiewicz *et al*., LAMTOR2 (p14) controls B cell differentiation by orchestrating endosomal BCR trafficking. *Front. Immunol.* **10**, 497 (2019).
79. S. Wang, C. Hu, F. Wu, S. He, Rab25 GTPase: Functional roles in cancer. *Oncotarget* **8**, 64591–64599 (2017).
80. C. Hu, B. Chen, Y. Zhou, Y. Shan, High expression of Rab25 contributes to malignant phenotypes and biochemical recurrence in patients with prostate cancer after radical prostatectomy. *Cancer Cell Int.* **17**, 45 (2017).
81. H. Jiang *et al*., Knockdown of hMex-3A by small RNA interference suppresses cell proliferation and migration in human gastric cancer cells. *Mol. Med. Rep.* **6**, 575–580 (2012).
82. D. Yang, Y. Jiao, Y. Li, X. Fang, Clinical characteristics and prognostic value of MEX3A mRNA in liver cancer. *PeerJ* **8**, e8252 (2020).